Experimental spectro-angular mapping of light distribution in turbid media

Serge Grabtchak
Tyler J. Palmer
Florian Foschum
Andre Liemert
Alwin Kienle
William M. Whelan

SPIE

Experimental spectro-angular mapping of light distribution in turbid media

Serge Grabtchak,[a,b,c] Tyler J. Palmer,[a] Florian Foschum,[d] Andre Liemert,[d] Alwin Kienle,[d] and William M. Whelan[a,e]
[a]University of Prince Edward Island, Department of Physics, Charlottetown, PEI Canada C1A 4P3
[b]Dalhousie University, Department of Electrical and Computer Engineering, Halifax, NS Canada B3J 1Z1
[c]Dalhousie University, Department of Physics, 6310 Coburg Road, Halifax, NS Canada B3H3J5
[d]Institut für Lasertechnologien in der Medizin und Meßtechnik an der Universität Ulm, Helmholtzstr.12, D-89081 Ulm, Germany
[e]Atlantic Veterinary College, Department of Biomedical Sciences, Charlottetown, PEI Canada C1A 4P3

Abstract. We present a new approach to the analysis of radiance in turbid media. The approach combines data from spectral, angular and spatial domains in a form of spectro-angular maps. Mapping provides a unique way to visualize details of light distribution in turbid media and allows tracking changes with distance. Information content of experimental spectro-angular maps is verified by a direct comparison with simulated data when an analytical solution of the radiative transfer equation is used. The findings deepen our understanding of the light distribution in a homogenous turbid medium and provide a first step toward applying the spectro-angular mapping as a diagnostic tool for tissue characterization. © 2012 Society of Photo-Optical Instrumentation Engineers (SPIE). [DOI: 10.1117/1.JBO.17.6.067007]

Keywords: radiance spectroscopy; diffuse scattering; turbid media; spectro-angular mapping; biological phantoms; tissue diagnostics.

Paper 12055 received Jan. 27, 2012; revised manuscript received May 1, 2012; accepted for publication May 10, 2012; published online Jun. 8, 2012.

1 Introduction

Biological tissues are scattering (i.e., turbid) media where light undergoes diffusion-like transport. It presents a significant challenge for optical imaging and tissue characterization. Radiance-based (also known as point radiance spectroscopy) techniques have been used for the study of liquid phantoms and biological tissues since 1997.[1–5] Radiance defines a variation in the angular density of photons impinging on a selected point in tissue. To obtain radiance data, a specially constructed optical probe with a well-defined angular detection window must be rotated along its axis. Interpretation of results is usually done in conjunction with either Monte-Carlo simulation[1] or various approximations when solving the radiative transfer equation (RTE).[2,3] Extraction of optical properties of media under study from radiance measurements has also been demonstrated.[4,5] Irrespective of the analysis framework, radiance-based techniques have not received as much attention as fluence-based methods.[6–15] Other than more complex experimental set-ups, another reason for this might be that radiance is considered merely a sub-set of the fluence and provides some additional information that cannot be fully appreciated when applied to turbid media in practice. Since fluence measures photons impinging on a detector in the entire 4π solid angle, it does not catch the subtle angular variations in photon distributions in the vicinity of a detector.

However, such knowledge of the angular distribution of photons impinging from specific directions at a selected location inside biological tissues would be beneficial in establishing conditions for drug illumination in photodynamic therapy (PDT), optimizing light delivery in gold-nanoparticles mediated thermal therapy or spatially-resolved detection of optical inhomogeneities by optical imaging modalities. As opposed to fluence, radiance has a capacity of providing a full spectral analysis in the angular domain that yields a spatial resolution. This is an attractive feature because of the extra parameter space radiance-based diagnostic techniques may be able to lessen a burden of fluence-based, highly complex image reconstruction algorithms (inverse problem) that are used in the diffuse optical tomography (DOT).[16,17] It is well known that combining DOT with other imaging modalities like magnetic resonance imaging (MRI) improves the resolution and accuracy of reconstructed images by constraining the inverse problem.[17] Moreover, non-linear image reconstruction algorithms are required when there is a large discrepancy between the refractive index of the inhomogeneity and the surrounding medium (e.g., Au nanoparticles in tissues). While DOT is usually performed at boundaries of interested regions, interstitially applied radiance can provide a look at tissues and organs from inside. However, before it becomes a reality, a capability of radiance of producing spectro-angular information in a compact but informative form amenable to use in tissue diagnostics and imaging should be demonstrated. Establishing such a form and its analysis has been the main motivation behind the current work. Our second objective was to validate a recently developed[18] radiance model based on the analytical solution of RTE by applying it for solving the forward problem and comparing generated patterns with experimental ones.

In our previous studies,[19–21] we already took further steps with radiance-based techniques by showing that radiance is capable of detecting localized inclusions of gold nanoparticles in Intralipid-1%. The system with inclusions as well as most biological tissues of interest has varying degrees of structural inhomogeneity that in most cases translates to an optical inhomogeneity. A goal of all optical imaging modalities is to detect local properties of tissues and provide information about location and optical parameters of various inclusions that can cover a wide range from malignancies to exogenous optical chromophores. In order to optimize the detection of inclusions,

Address all correspondence to: Serge Grabtchak, University of Prince Edward Island, Department of Physics, Charlottetown, PEI Canada C1A 4P3. Tel: (902) 566-6078; Fax (902)566-0483; E-mail: sgrabtchak@upei.ca

however, knowledge of intricate details of light propagation in the background medium is required. A simple example may be helpful. It is obvious that in a homogenous, turbid medium light propagation and detection are governed by (mostly) scattering properties of the medium. Adding a localized absorptive inclusion would change properties only locally (i.e., in a vicinity of the inclusion). However, its signature can be detected almost anywhere inside the turbid medium via scattering still originating from the background medium. In this example, background scattering can be thought of as a carrier, and the localized absorber as a perturbation or modulation of the carrier. Hence, for all imaging modalities homogenous phantoms with known optical properties provide both quantitative and qualitative input for interpretation of complex images. Therefore, while performing radiance measurements in a well characterized substance, like Intralipid-1% may appear trivial, our goal was not to reincarnate a way of extracting optical parameters that has been already established for radiance. Instead, we examine how optical properties of the background material are encoded in complex measured patterns, how the patterns are affected by the source-detector separation and support with modeling experimental results of increasing complexity that are not obvious or intuitive. This lays down a solid foundation for studying more complex systems with inclusions. To take full advantage of the information content supplied by radiance, we propose a multidimensional mapping approach to the analysis of radiance results from Intralipid-1% by combining data from spectral, angular, and spatial domains. Mapping provides a unique way to look at the wavelength-dependent angular distribution of light inside biological phantoms. As a result, a wealth of information is presented in a convenient and easily accessible way in a form of spectro-angular maps, or snapshots, that can serve as diagnostic tools when applied to biological tissues. We exploited the wide VIS/NIR range of the white light spectroscopy for spectral analysis of Intralipid-1%. Measurements were done over the entire 360 deg angular range and covered a source-detector separation distance from 6.5 to 30.5 mm. Intralipid was selected as a test bed for the current study because it is a well-characterized liquid phantom. Possible applications of the spectro-angular mapping in tissue diagnostics and imaging were discussed.

2 Materials and Methods

2.1 Point Radiance Spectroscopy Set-Up

The details of the experimental set-up for radiance measurements in Intralipid-1% have been extensively described elsewhere.[19,20] A schematic of the experimental setup is shown in Fig. 1. Briefly, the phantom Lucite box (with blackened 18 cm walls) was filled with Intralipid-1% solution and accommodated a fiber with a 800-micron spherical diffuser (connected to a white light source) and a 600-micron side firing fiber (the radiance detector). The side firing fiber had a well-defined angular acceptance window of ~10 deg in water. Both fibers were threaded through ~1.1 mm stainless steel tubes for mechanical stability. Source-detector separation was varied from 6.5 to 30.5 mm in various measurements. The radiance profiles were acquired by rotating the detector over a 360 deg range with a 2 deg step. The side firing fiber was connected to a USB 4000 spectrometer (Ocean Optics) that collected spectra at every angular step. Intralipid-1% solution was prepared by volume dilution of the stock solution of Intralipid-20% from Sigma Aldrich Canada.
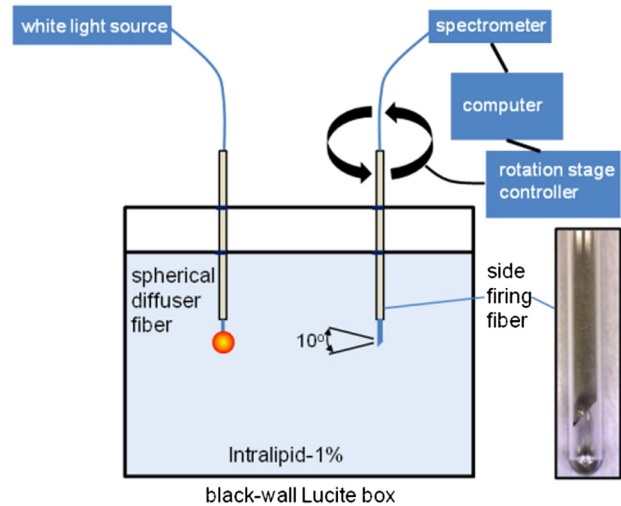
Fig. 1 The schematic of the experimental setup. The inset shows a tip of the side firing fiber.

2.2 Set-Ups For Basic Characterization of Intralipid-1%

Basic characterization included measurements of the absorption coefficient ($\mu_a(\lambda)$), the reduced scattering coefficient ($\mu_s'(\lambda)$), and the scattering coefficient ($\mu_s(\lambda)$) for the Intralipid sample using the collimated transmission and the spatially resolved reflectance set-ups. The experimental set-ups and the measurement procedure have been described previously.[22,23] Anisotropy factor, $g(\lambda)$, was calculated as $g(\lambda) = 1 - \mu_s'(\lambda)/\mu_s(\lambda)$.

Figure 2 displays optical parameters of Intralipid-1% that were obtained from the basic characterization measurements: $\mu_s'(\lambda)$ (a), $\mu_a(\lambda)$(b), $\mu_s(\lambda)$(c), and $g(\lambda)$(d). Error bars for the reduced scattering coefficient combine the standard deviation of three measurements and 5% systematic error expected by using the diffusion theory for retrieving the optical properties from the measurements. The absorption coefficient demonstrates a good agreement with the absorption of water for wavelengths >700 nm.[24] For wavelengths <600 nm, the absorption of soy bean oil is the main contribution to the measured absorption spectrum.[22] Both the scattering and the reduced scattering coefficients are well described by the power law (fitted red solid lines). The error for the scattering coefficient (not shown) equals the standard deviation of five measurements.

2.3 Modeling Approach

A recently derived[18] analytical solution of the RTE for the radiance caused by an isotropic light source placed inside an infinitely extended anisotropic scattering medium was used for comparison with experimental data. Because of the excellent agreement between the solution of the RTE and the Monte-Carlo method using the Henyey-Greenstein phase function, the proposed $P_N(N = \infty)$ method was considered as a reference for the present study. We chose a sufficiently high number of summation terms $N = 17$ to closely match the P_∞ approximation.

For the purpose of this article, the radiance (I) has been expressed as a function of optical properties of the Intralipid sample [$\mu_a(\lambda)$, $\mu_s'(\lambda)$ and $g(\lambda)$] that can be considered as fixed parameters. These parameters were obtained directly from the basic characterization measurements. The radiance is also a function of the cosine of the angle between the direction
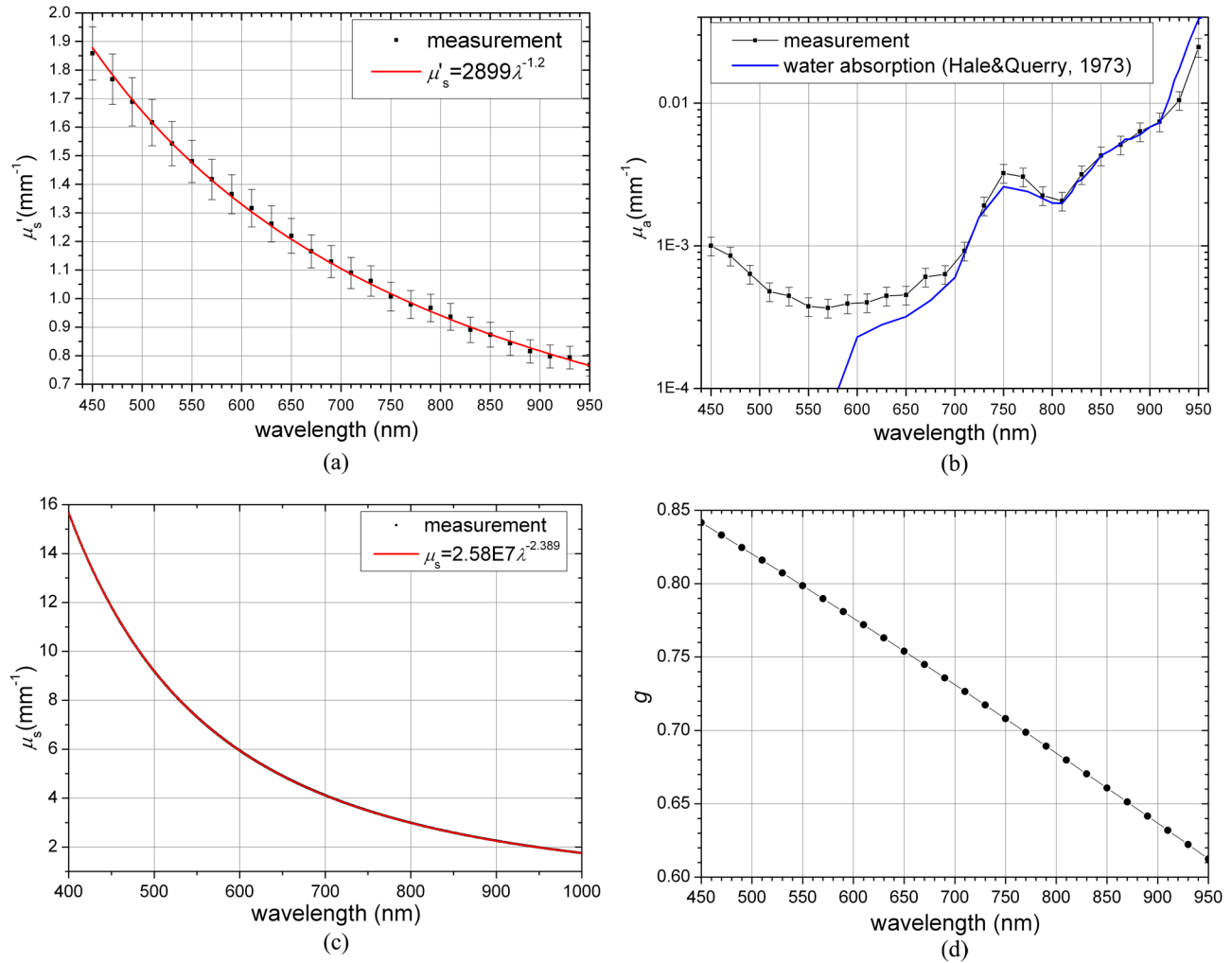
Fig. 2 Optical parameters of Intralipid-1% from basic characterization measurements: (a) the reduced scattering coefficient, $\mu_s'(\lambda)$, (b) the absorption coefficient, $\mu_a(\lambda)$, c) the scattering coefficient, $\mu_s(\lambda)$, d) the anisotropy factor, $g(\lambda)$.

of propagation and the direction of scattering (θ), the distance between the source and the detector (r), and the wavelength (λ) (implicitly) that we consider as variables. This distinction between the parameters and the variables is of artificial origin that merely facilitates a direct comparison with experimental data. For example, by fixing all parameters and variables except for the wavelength, we can obtain the spectral radiance as a function of wavelength. Similarly, by fixing everything but the angle we can obtain the angular radiance. By analogy, the distance dependent radiance can be obtained by fixing everything but the source-detector separation.

The radiance obtained from the diffusion equation (P_1 approximation) is known to be valid under certain limited conditions, and it has been discussed extensively in the literature.[25] The reduced scattering coefficient must be much larger than the absorption coefficient, and the product of the reduced scattering coefficient and the measurement distance should be large ($\gg 1$). Also, the discrepancies for the angular radiance $I(\theta)$ obtained from P_1, P_3, P_∞, and Monte-Carlo simulations are well known and documented.[18] Less studied is the distance dependent radiance, $I(r)$, its combined analysis in spectral and angular domains, and applicability of P_1 approximation for its description. For example, absolute distance dependent measurements of the fluence are known to provide the absorption and the reduced

scattering coefficients thanks to the simplistic expression for the fluence.[6,8] An attractive feature of the P_1 approximation is that it offers a clear physical framework for data interpretation and straightforward parameter extraction during a fitting procedure. We tested the applicability of the diffusion approximation in the current study by fitting both simulated and experimental distance dependent data to the expressions derived from the diffusion approximation for radiance:

$$I(r, \theta, \lambda) = \frac{P_0}{(4\pi)^2 \cdot D(\lambda)}$$

$$\cdot \left\{ 1 + 3 \cdot \left[\frac{D(\lambda)}{r} + \mu_{\text{eff}}(\lambda) \cdot D(\lambda) \right] \cdot \cos\theta \right\}$$

$$\cdot \frac{\exp\left[-\mu_{\text{eff}}(\lambda) \cdot r \right]}{r}, \tag{1}$$

where P_0 is the source power, $D(\lambda) = 1/3(\mu_s'(\lambda) + \mu_a(\lambda))$ is the diffusion coefficient [mm], and $\mu_{\text{eff}}(\lambda) = \sqrt{\mu_a(\lambda)/D(\lambda)}$ is the effective attenuation coefficient [mm^{-1}]. Our approach was to 1. obtain the absorption coefficient, the scattering coefficient, and the reduced scattering coefficient from basic characterization measurements; 2. simulate experimental data with the P_∞ approximation using three basic parameters and the anisotropy

factor; 3. calculate $D(\lambda)$ and $\mu_{\text{eff}}(\lambda)$ using the absorption and the reduced scattering coefficients obtained from basic characterization measurements; and 4) fit the simulated and the experimental radiance to Eq. (1) to recover $D(\lambda)$ and $\mu_{\text{eff}}(\lambda)$. In order to avoid introducing a third parameter into fitting that is related to the source power, we also derived an expression for a ratio of two radiances (one taken at the reference distance, r_0) for $\theta = 0$:

$$\frac{I(r)}{I(r_0)} = \frac{\left\{\frac{1}{D(\lambda)} + 3 \cdot \left[\frac{1}{r} + \mu_{\text{eff}}(\lambda)\right]\right\} \cdot \frac{\exp[-\mu_{\text{eff}}(\lambda)\cdot r]}{r}}{\left\{\frac{1}{D(\lambda)} + 3 \cdot \left[\frac{1}{r_0} + \mu_{\text{eff}}(\lambda)\right]\right\} \cdot \frac{\exp[-\mu_{\text{eff}}(\lambda)\cdot r_0]}{r_0}}. \quad (2)$$

We assigned the shortest source-detector separation from our measurements to be r_0. Equation (2) was also used in the fitting procedure.

3 Results and Discussion

3.1 Radiance at a Fixed (12 mm) Source-Detector Separation

As a starting point of most tissue or phantom characterizations, measurements are usually performed at a fixed source-detector separation. Detailed radiance measurements were done at a 12 mm source-detector separation. Filling the phantom box with the Intralipid medium changes the spectrum collected by the detector ($I_{\text{Intralipid}}$) as compared with the one measured in air (I_{air}). To exclude spectral features of the white light source and the detector, the ratio of two spectra, $I_{\text{Intralipid}}/I_{\text{air}}$ was constructed. It is plotted in Fig. 3(a) as an experimental spectral radiance. Two spectral profiles of the radiance are shown: one taken with the detector facing the light source (corresponding to 0 deg polar angle) and the other with the detector facing opposite the light source (corresponding to 178 deg polar angle). (Experimental data were corrected by a difference in light refraction on the curved fiber surface in air and water). The plot also shows two theoretical curves that were computed using the analytical radiance model (P_∞) with input parameters from the basic characterization measurements as shown in Fig. 2. Once a single amplitude scaling factor is introduced, the agreement between the experimental and theoretical data is quite good. A scaling factor is required because modeling was done using a unit power, and no absolute calibration of radiance

in experiment was performed. All spectral profiles show characteristic features of water absorption: a dip at 750 nm and a steep decrease toward 1000 nm. The peak around 550 nm is formed by overlapping of decreasing with wavelength absorption of Intralipid and increasing with wavelength water absorption (see Intralipid absorption spectrum in Fig. 2). Since this shape is a convolution of responses of two chromophores (soybean and water) with different absorption coefficients, the overall absorption spectrum of the turbid medium will be a summation of products of the corresponding absorption coefficient and the effective optical path taken by photons before reaching the detector for every chromophore. However, because of the multiple scattering the spectral shape will be a distance-variant feature.

Radiance pattern as in Fig. 3(a) can be considered a function of three parameters: the absorption coefficient, the reduced scattering coefficient, and the anisotropy factor. The excellent agreement between the experiment and modeling indicates a possibility of parameter extraction from experiments by developing a suitable fitting algorithm. In order to recover three independent parameters, one would need technically only three relations. Because these parameters are distance- and angle-invariant, the robustness of the recovery will be greatly improved by fitting at the same time not three but all experimental angular-dependent radiance data sets (180 in this study). Multiple curve fitting can be a challenge, but a multi-spectral approach that has similar issues is commonly used in DOT.[17] Hence, once achieved, it can bring radiance-based cw techniques closer to those of time- and frequency-domain in terms of being able to separate absorption from scattering in a single measurement for a single source-detector pair.

The angular radiance (measured and computed) for two selected wavelengths (550 nm and 850 nm) is shown in Fig. 3(b). In order to facilitate the comparison, the data were normalized to the maximum value at 0 deg. Experimental curves demonstrate slightly lower values than theoretical ones. The maximum difference occurs at 178 deg and is greater for shorter wavelengths ($\sim$8% for 550 nm and $\sim$4% for 850 nm). The difference is due to a number of factors. A finite width of a $\sim$1.1 mm diameter stainless steel tube that accommodates the side firing fiber obscures a path of photons in Intralipid. In particular, photons that would have reached the fiber after being backscattered undergo
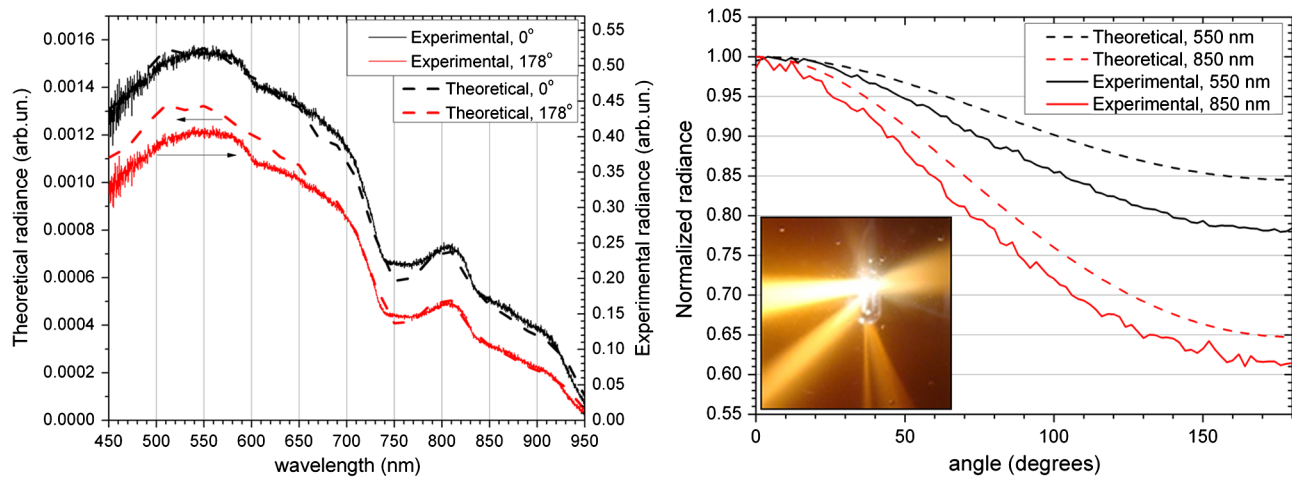
Fig. 3 (a) Spectral radiance (experimental and theoretical) for Intralipid-1% at 0 deg and 178 deg. (b) Angular radiance (normalized, experimental and theoretical) for Intralipid-1% for 550 nm and 850 nm. Inset: light beams coming from the side firing fiber.

additional scattering and absorption when hitting the tube. Because of a three-dimensional nature of scattering, the entire part of the tube immersed into Intralipid acts as a perturbation. As a result, the experimental radiance detected at 178 deg is lower than the theoretical one. To confirm this effect we replaced the 600-μm side firing fiber in the 1.1 mm tube with a bare (no tube) 400 μm diameter side firing fiber and repeated the angular measurements. The resulting values for the radiance measured at 178 deg were then greater than the theoretical values: by ~7% and ~15% for 550 and 850 nm, respectively. The increase is accounted by a contribution of light that does not undergo a total internal reflectance in the fiber tip. The inset in Fig. 3(b) demonstrates the light emission from the side firing fiber when coupled to a white light source in a weakly scattering medium. Aside from the main beam coming at ~90 deg angle to the left, there are three more weak beams. The one that exits at ~90 deg angle to the right is most likely a Fresnel reflection of the main beam at the glass/air interface inside the cap. Two other beams are formed by light that does not undergo total internal reflection (as confirmed by a manufacturer). It means that light would be able to couple back to a fiber following these pathways. All three beams contribute to the measured radiance by providing an increased background and a weakened angular sensitivity. By placing a Si detector in air close to the fiber top and the fiber side, we estimated the amount of light leaking through the top to be within ~12% range of the total signal which agrees well with the measured differences. All the fibers tested have light patterns similar to the one shown on the inset of Fig. 3(b). It appears that the contribution from all secondary beams was almost overcompensated by the blocking effect of the tube showing radiance values less than expected for the 600 μm fiber in the tube. Once the tube was removed and the thinner 400 μm fiber was tested, the contribution from the secondary beams became more evident. To clarify the matter it is worth noting that the total amplitude of a signal collected by the 400 μm fiber is always less than that collected by the 600 μm fiber. All further experiments reported in the article were performed with the 600 μm side firing fiber in the tube, therefore, accepting up to ~8% difference with modeling results.

Since both experimental spectral and angular radiance data sets have been validated with modeling, they can be considered as elemental building blocks for more complex representations. For 360 deg spectral collection, Intralipid data were converted into an "Intralipid" matrix (angle versus wavelength) with individual spectra serving as columns. Spectral radiance was measured every 2 deg in (0 to 360) deg interval in the same spectral range for all angles. An "air" matrix was constructed by filling all (angular) columns with the spectrum measured in air at 0 deg. The result of the division of two matrices (Intralipid/air) is presented as a contour plot (normalized) in Fig. 4(a) and demonstrates light distribution inside Intralipid-1%. This type of referencing to air does not introduce any angular skew but consistently removes instrumental spectral features. Contour lines and same color represent equal intensity of light. The light wavelengths that undergo the least attenuation in the Intralipid correspond to red color. Contour lines clearly delineate the transmission peaks (i.e., around 550 nm) and the valleys (i.e., around 740 nm). Figure 4(a) not only shows all spectral features observed in Fig. 3(a) but presents the corresponding angular distribution. An angular spread due to multiple scattering of light is clearly observed. The effect of light spreading in Intralipid can be monitored by fixing the wavelength on the Y-axis and following the

(a)

(b)
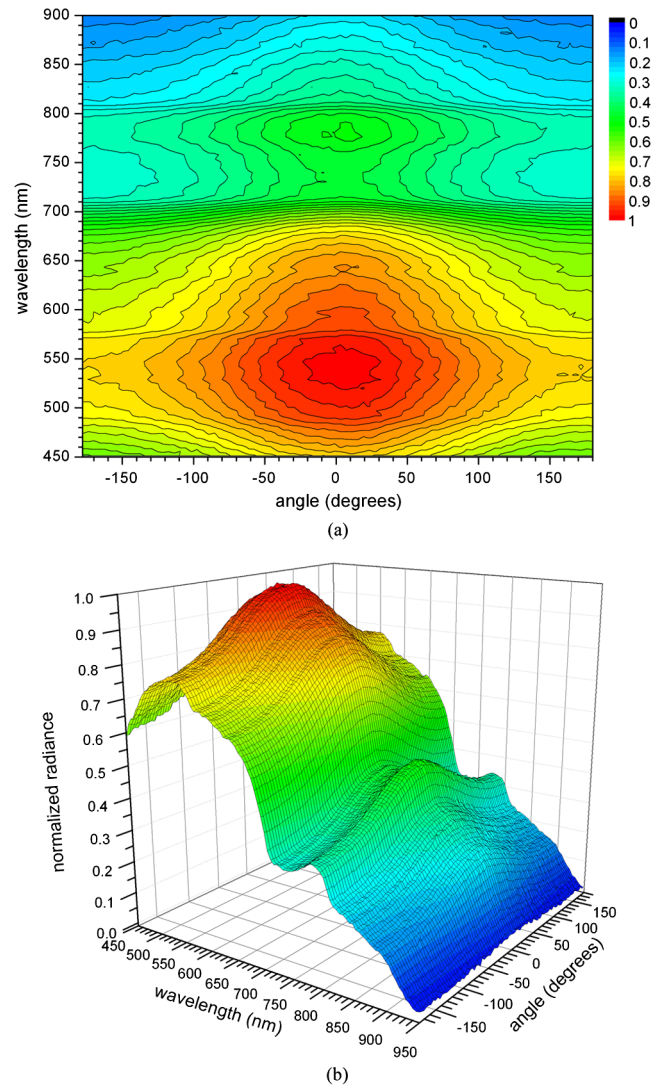
Fig. 4 (a) Experimental contour plot (normalized) of the spectro-angular distribution of radiance in Intralipid-1%. (b) Experimental surface plot (normalized) of the spectro-angular distribution of radiance in Intralipid-1%. All for 12 mm source-detector separation (the same color coding for both plots).

intensity (color) variation with angle. Such angular information is not achievable with fluence measurements.

We found that different Intralipid batches from the same manufacturer, Sigma-Aldrich Canada exhibit some variations in the spectral response in the 450 to 550 nm range. This range is very sensitive to the Intralipid composition which yields a different absorption. All wavelengths exhibit the maximum of light distribution along a 0 deg direction that is consistent with a preferential forward scattering in a homogenous medium. Cross-sections of the surface plot along Y-axis at constant X (angle) produces spectral profiles similar to those shown in Fig. 3(a). Sectioning the plot at a constant Y-axis (wavelength) along X-axis generates angular radiance distributions similar to those shown in Fig. 3(a). A 2-D analysis of Fig. 4(a) provides for the identification of the wavelength and the direction of the least attenuation, i.e., ~550 nm and 0 deg, correspondingly.

Details of the spectral variation with angle become more evident when data are presented in the form of a surface plot

in Fig. 4(b) that allows seeing more clearly a spectral content. A symmetrical around 0 deg distribution of light in the Intralipid phantom is not surprising giving a homogenous composition of the solution. As one can see from Fig. 4(b), other than a reduction in intensity, the backscattered spectrum undergoes relatively minor changes in overall shape compared to the forward scattered spectrum. Therefore, the nature of the signals is the same and reflects a distribution of the photon density due to an increased optical pathlength of backscattered photons.

A comparison of Fig. 4(a) and 4(b) with a similar representation of radiance obtained from modeling under P_∞ approximation [Fig. 5(a) and 5(b)] demonstrates a remarkable degree of correspondence between these complex plots. Since experimentally obtained data are not bound to any approximations (diffusion in particular), a good correspondence to modeling under P_∞ approximation indicates that the spectro-angular approach is a valid way to present and analyze radiance data. It is important to note that simulated radiance does not involve any referencing and provides absolute values. As was described
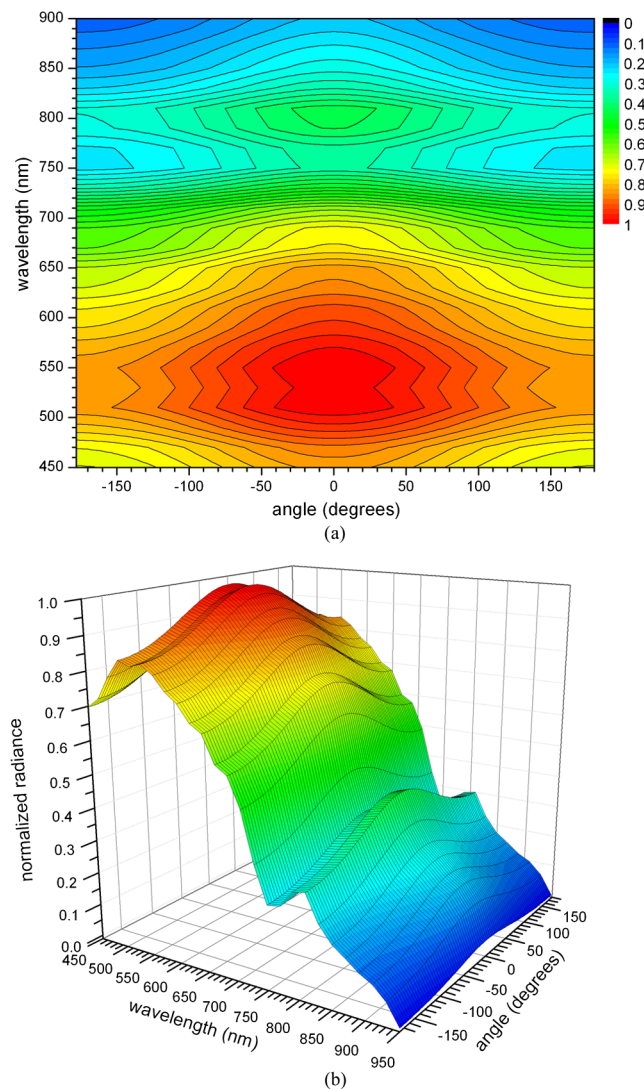
earlier, experimentally obtained radiance is a ratio of two spectra and therefore, has a relative nature.

While for homogenous phantoms and tissues quantitative information about optical properties can be extracted from spectro-angular snapshots via numerical analysis by solving the inverse problem (which is beyond the scope of the current article), some qualitative trends can be predicted when comparing several snapshots. Spectral variations due to changes in wavelength-dependent absorption coefficients are easily seen in the forward scattering direction where the signal is maximal. It can be applied to track changes in tissue properties as a result of coagulation or drug action (i.e., before and after PDT). On the other hand, an increase in the backscattered signal would be indicative of a decreased anisotropy factor, decreased absorption coefficient, or increased reduced scattering coefficient.[1]

It is evident that a spectro-angular snapshot of a homogenous turbid medium has a symmetric pattern exhibiting a maximum for forward scattered photons (i.e., 0 deg). As was shown earlier,[21] introducing a localized optical inhomogeneity via Au nanoparticles disrupts the symmetry and produces a new spectroscopic signature in the direction of the inhomogeneity. Therefore, in a single 360 deg scan a single radiance detector positioned at a fixed distance from a single light source can map a localized inhomogeneity in the spectro-angular domain. Such a target inhomogeneity cannot be localized or identified from a single fluence measurement. That is why various combinations of multiple sources and/or detectors are employed in DOT imaging to visualize the inhomogeneity in X,Y-domain using selected wavelengths of light. Hence, trade-offs between multiple point superficial measurements required by DOT to obtain an accurate image of the inclusion at a selected wavelength and a single point interstitial radiance scan to achieve angular localization of the target should be clearly understood. Moreover, spectro-angular mapping using radiance is not a typical imaging approach, but rather provides additional spatial information absent in other spectroscopic techniques.

Many *in vivo* PDT treatments in prostate, including treatment planning and dosimetry, utilize interstitial fluence measurements,[11,14,26] with source and probe fibers in various combinations inserted into multiple tissue segments, thus increasing invasiveness. Alternatively, radiance applications for prostate characterization hold the potential for requiring only a single interstitial placement of a rotating radiance probe in the urethra and an illumination source in the rectum, to acquire spatial information about spectral properties of the surrounding tissue. This illumination-detection geometry can be considered more favorable than the fluence-based approach because it offers a minimally invasive application for prostate diagnostics or PDT monitoring. Hence, radiance may be a viable alternative, minimally invasive method for tissue diagnostics especially when offered as an endoscopic technique.

It is known that prostate tissue heterogeneity represents an important problem for PDT dosimetry because it contributes to the effective attenuation coefficient averaged over a large portion of the prostate gland that can complicate the delivery of the desired PDT dose to tissues. Translating detecting fibers along the thickness of the prostate gland or using multiple sites for combined illumination-detection fluence measurements can provide indications of a presence of such heterogeneity rather than incorporating it in a tissue model. However, spectro-angular mapping with radiance may be better suited for characterization of localized heterogeneities or inclusions, providing

Fig. 5 (a) Simulated contour plot (normalized) of the spectro-angular distribution of radiance in Intralipid-1%. (b) Simulated surface plot (normalized) of the spectro-angular distribution of radiance in Intralipid-1%. All for 12 mm source-detector separation (the same color coding for both plots).

the needed spatial information in a less invasive way. Radiance cannot replace fluence in PDT applications at the current stage, but with developments in radiance-based dosimetry and treatment planning algorithms it may serve as a new basis for PDT.

3.2 Distance-Dependent Measurements in Intralipid-1%

Tissue diagnostics and imaging require a clear understanding of how measured optical radiance is affected by variations in the source-detector separation. Distance-dependent radiance measurements were completed by changing the source-detector separation from 6.5 to 30.5 mm with a 2 mm step and performing either a full 360 deg angular scan at every step or keeping the angle fixed in certain experiments. Initially, we considered the case when the detector is facing the light source (i.e., 0 deg angle, no rotation).

We started the study with simulating distance-dependent radiance for the same source-detector separation range as in the experiment. The spatial dependencies for selected wavelengths are shown in Fig. 6(a) with colored symbols. We tested the applicability of the expression for the distance dependent radiance under diffusion approximation and fitted simulated data with Eq. (1) using $D(\lambda)$ and $\mu_{\mathrm{eff}}(\lambda)$ as parameters. Solid lines in Fig. 6(a) represent results of fittings to Eq. (1) with the unit power ($P_0 = 1$). Since all the parameters of Intralipid-1% have been available from the basic characterization experiments, we also calculated $D(\lambda)$ and $\mu_{\mathrm{eff}}(\lambda)$ from the experimental values shown in Fig. 2. Fittings produced excellent agreement with experimental values. For example, for 450 nm wavelength the values were: reduced $\chi^2 = 3.1 \times 10^{-6}$, $\mu_{\mathrm{eff\ model}}(450) = 0.07502 \pm 6.8 \times 10^{-5}$ mm^{-1}, $D_{\mathrm{model}}(450) = 0.17737 \pm 2.5 \times 10^{-4}$ mm and $\mu_{\mathrm{eff\ exp}}(450) = 0.07468$ mm^{-1}, and $D_{\mathrm{exp}}(450) = 0.17926$ mm. A full comparison for $\mu_{\mathrm{eff}}(\lambda)$ is shown in Figure 6(b) where the solid line corresponds to values directly calculated from basic characterization measurements and red open circles—to values from fittings of the simulated radiance. Therefore, even though simulations were done under the P_∞ approximation, distance dependent radiance can be described well by the radiance under diffusion approximation allowing for important parameter extraction. (It is important to emphasize

that the diffusion approximation still fails in providing an adequate description of angular dependent radiance).

In experiments, the input source power is not unity. Moreover, providing calibrated absolute radiance is a difficult task. To circumvent the problem, we explored the concept of relative measurements that would cancel the dependence on P_0 but preserve two optical parameters of interest. For this purpose we divided all simulated radiance values by the value at the shortest distance, i.e., 6.5 mm and fitted the normalized distance-dependent radiance to Eq. (2). In spite of an apparent simplicity of the approach and encouragingly small reduced χ^2, the results of fitting were not as expected: $\chi^2 = 5.7 \times 10^{-8}$, $\mu_{\mathrm{eff}}(450) = 0.07451 \pm 1.9 \times 10^{-5}$ mm^{-1}, and $D(450) = 0.227 \pm 0.001$ mm. The value of the slope (i.e., which represents the effective attenuation coefficient) was successfully recovered, however; the diffusion coefficient error was ~26%. The error increased up to ~80% for longer wavelengths. Apparently, normalization leads to an error accumulation at every fitting step which is manifested in the parameter responsible for the amplitude [i.e., $D(\lambda)$]. Finally, an attempt to introduce a third unconstrained parameter to the model (that would recover P_0) of non-normalized radiance data failed to recover P_0 and $D(\lambda)$ but again yielded accurate values for $\mu_{\mathrm{eff}}(\lambda)$. Extending the source-detector range up to 100 mm distance in simulations increased the dynamic range of radiance up to ~10 orders of magnitude but did not improve the recovery of P_0 and $D(\lambda)$. Hence, in the analysis of the distant-dependent experimental radiance, our focus was on the recovery of $\mu_{\mathrm{eff}}(\lambda)$ using the normalization approach and a two-parameter model.

Fitting experimental distance dependent normalized radiance produced results almost indistinguishable from modeling. Values of the effective attenuation coefficient extracted from the experimental radiance are presented in Fig. 6(b) as triangles. Again there is excellent agreement between the actual values (from basic characterization measurements) and those from the fits of both simulated and experimental radiance.

We applied the same analysis to the radiance obtained at 178 deg. In principle, due to the isotropy of the medium, the effective attenuation coefficient does not depend on the angle of detection. Indeed, the values of $\mu_{\mathrm{eff}}(\lambda)$ obtained from experimental backscattering data were similar to those shown in Fig. 6(b). Therefore, a rate of radiance change with distance
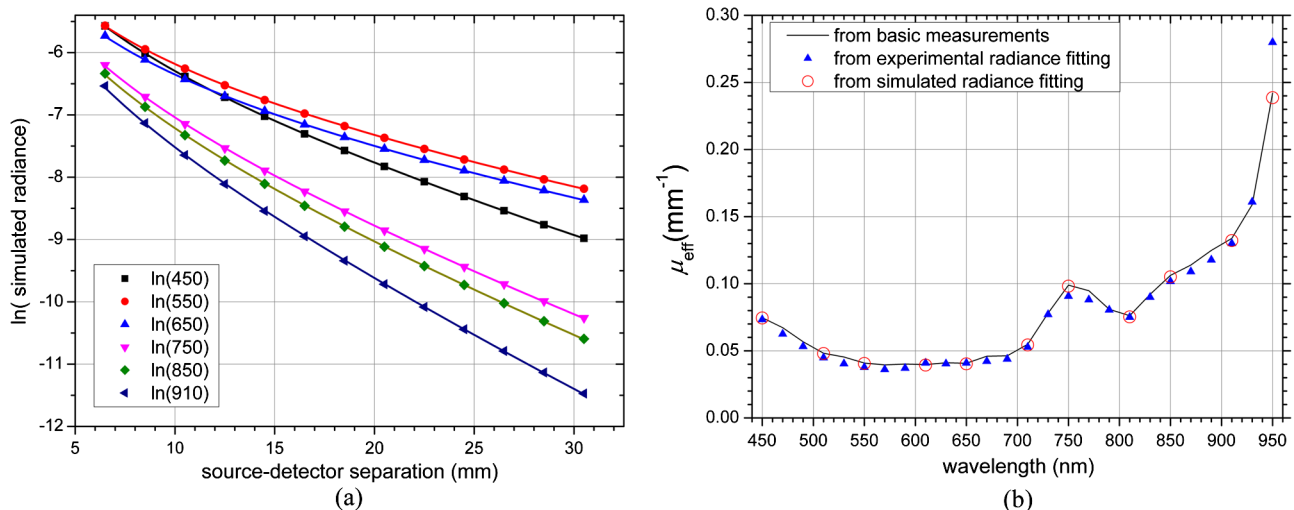
Fig. 6 (a) Simulated distance dependent radiance for selected wavelengths in Intralipid-1%. (b) The effective attenuation coefficient of Intralipid-1%.

is identical for all observation angles and equal to the effective attenuation coefficient for a homogenous medium. This approach offers the possibility of obtaining angular variations in the effective attenuation coefficient or its analogy for turbid media with a localized optical inhomogeneity.

The spectral shape of the effective attenuation coefficient, as observed in Fig. 6(b) carries important information about the wavelength corresponding to the least attenuation inside turbid media. While its shape resembles the absorption coefficient of Intralipid, it is distorted due to the contribution of the reduced scattering coefficient. It is the effective attenuation coefficient and its spectral shape that are ultimately responsible for the variation in radiance with distance. Such a variation is presented in Fig. 7. Continuing the analysis in multiple domains, we combined experimental distance-dependent data measured at 0 deg into a spectro-spatial contour plot as in Fig. 7 (note a log scale for radiance intensity variations). Modeling produces almost analogous plot (data not shown due to space limitations). In Fig. 7, the light wavelengths that are less attenuated are represented by a red color map. According to Fig. 7, the optimal transparency window for Intralipid-1% is in the 500 to 700 nm range. Working in the 700 to 900 nm spectral range should be avoided because of the detrimental impact of water absorption. In biological tissues, one of the important chromophores that defines the limits of the biomedical transparency window is hemoglobin, and it is absent in the present study. Clearly, the actual range of the biomedical transparency window depends on the nature of chromophores involved and should not be taken for granted as "one-fits-for-all" model. We'd like to point to a very important distinction between the information content of Fig. 6(b) and that of Fig. 7. The effective attenuation coefficient is a computed quantity that is valid for conditions satisfying the diffusion approximation. On the other hand, spectro-spatial mapping of the distance-dependent radiance is obtained directly from the experiment and is not bound by any approximations. Therefore, it will be able to provide an important insight into details of light extinction in different directions inside turbid media even when a concept of the effective attenuation coefficient is not applicable. The selected distance range (6.5 to 30.5 mm) targets prostate probing
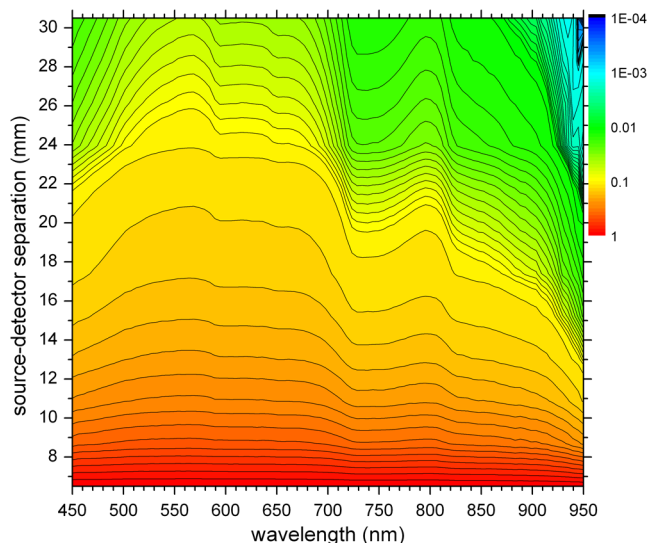
applications. For an average prostate diameter of 5 cm, illuminating through rectal wall and detecting with urethra-placed fiber will ensure probing prostate in a minimally invasive way. When a standard brachytherapy grid is used for interstitial placement of the source fiber in various locations of the prostate, spectro-spatial representation would allow determining the biomedical transparency window for the prostate, estimating the effective attenuation coefficient and relating spectral changes to distance. This information is likely useful for diagnostics and treatment planning. Fluence measurements done in the same geometry can also benefit from spectro-spatial analysis, especially when the diffusion approximation is not valid. It should be noted that both fluence and radiance measurements performed in this way share an increased degree of invasiveness because of a need of multiple distance measurements.

When spectro-angular representation is applied to the distance-dependent radiance, it enables a unique ability to visualize angular transformations in the radiance distribution with depth inside turbid media. Presenting intensity variations of radiance simultaneously in spectral, spatial, and angular domains in a single quazi-3D plot is extremely difficult. To demonstrate dynamics of changes in light distribution, we combined a series of experimental spectro-angular snapshots [similar to one shown in Fig. 4(a)] measured every 2 mm in a 6.5 to 30.5 mm source-detector separation range in a short animation with 12 frames (Video 1). To facilitate the comparison and smooth transformations, every individual spectro-angular snapshot (i.e., a frame) was normalized to a maximum signal. Therefore, the identical color code covers the same 0 to 1 range for all distances. The short animation demonstrates spectral and angular changes in a photon distribution as the detector moves away from the source. In addition to expected angular broadening due to multiple scattering effects, spectral changes also accompany variations in distance. Similar to the analysis done for a 12 mm source-detector separation, we confirmed all experimental plots via simulation (data not shown due to space limitations). The origin of spectral changes is analyzed below.

The first snapshot taken at shortest 6.5 mm source-detector separation somewhere resembles the one shown at Fig. 4(a).

Fig. 7 Spectro-spatial contour plot of experimental radiance (log scale) for distance-dependent measurements at 0 deg.
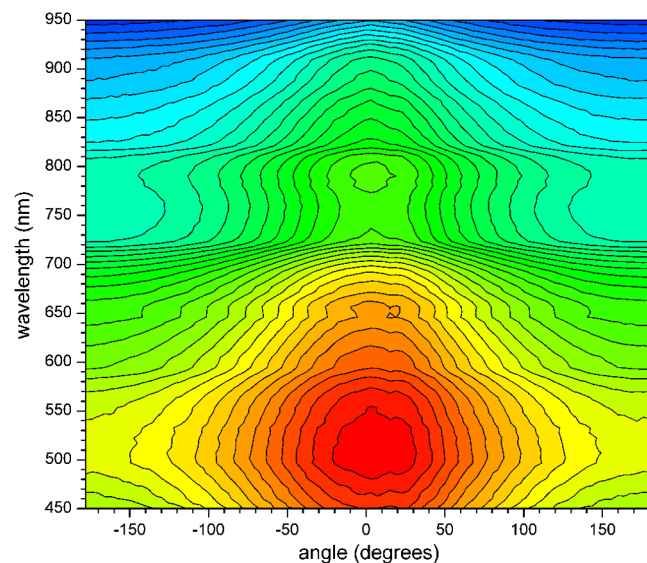
Video 1 Transformation of spectro-angular light distribution with distance in Intralipid-1% (from 6.5 to 30.5 mm, 2 mm step) (MPG, 2.6 MB) [http://dx.doi.org/10.1117/1.JBO.17.6.067007.1].

Since this approach removes spectral features inherent to the source and the detector, all signatures that are visible are due to Intralipid only. The spectrum measured at 6.5 mm shows a broadly defined maximum in the 480 to 550 nm range with a gradual slope towards the water absorption dip at 750 nm and a steeper slope starting around ~900 nm At short distances from the source, the effects of the two chromophores (soybean oil and water) on the transmission spectrum are not very distinct because photons reaching the detector interact with a relatively small volume of Intralipid around the source. Even though concentrations of both chromophores do not change, a relatively short effective optical pathlength is responsible for spectral changes. Therefore, the interaction between the photons and the medium can be relatively insensitive to weak absorption by chromophores at short distances. In the angular domain, the transmission peak spans a 50 deg. range (according to the first contour line) and rests on ~0.7 in magnitude background provided by backscattered photons.

The distribution obtained at 30.5 mm away from the source (Fig. 8) undergoes substantial changes. As was mentioned earlier, spectral features due to various absorption components become more prominent with distance. Because of the increased effective optical pathlength, photons interact with a larger volume of Intralipid. The transmission peaks become sharper and more well-defined because they are now bounded by regions of stronger absorption. At the same time, the relative amount of light contained in the spectral range >700 nm falls from ~50% to ~10%. Distance-dependent plots indicate that the transmission spectrum of Intralipid changes with distance, although the rate of change is expected to be less at very large distances. It implies that when translated to biological tissues one should not expect to deal with a universal spectrum that is distance-invariant and can be thought of as a characteristic fingerprint of a tissue. Rather, contributions from present chromophores will continuously reshape the spectrum with distance making it recognizable but not identical.

This effect, however, can be turned into a benefit by linking the distinct spectral and spatial evolutions to the source-detector separation and extracting a polar distance coordinate in addition to the angular one. This is important for solving the inverse problem when the accuracy of distance knowledge impacts values of recovered optical parameters, for example. Also, linking characteristic spectro-spatial changes to distance may help in determining a distance between a localized inclusion and a detector that is usually unknown but of high interest. Information reach spectro-angular data manifest two clear trends: angular broadening and spectral narrowing with distance. Rather than analyzing the distance behavior at any particular wavelength, we attempted to look at the behavior of the entire spectro-angular shape which would demonstrate some degree of universality while losing any explicit wavelength dependence. We've selected two contour lines (corresponding to 0.95 and 0.9 levels) from experimental spectro-angular contour plots and followed a distance variation of spectral ($\Delta\lambda$) and angular ($\Delta\theta$) ranges bounded by the outermost values in the contour lines. The results are presented in Fig. 9(a) and 9(b). The values of the spectral range ($\Delta\lambda$) versus distance can be independently predicted from a spectro-spatial plot of experimental transmission at 0 deg as in Fig. 7 after some modifications. A common feature of all spectro-angular snapshots is that the widest spectral range occurs at 0 deg for all contour lines. A modification of the plot from Fig. 7 included normalization to a maximum value at every
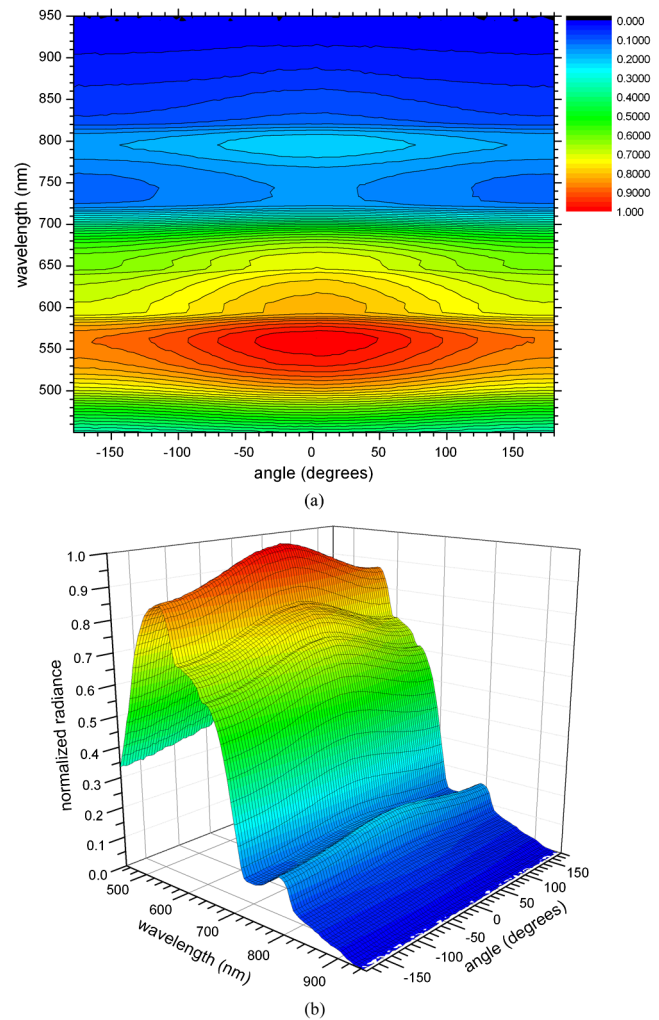
Fig. 8 Experimental contour plot of the spectro-angular distribution of radiance (a) and experimental surface plot of the spectro-angular distribution of radiance (b) in Intralipid-1% for 30.5 mm source-detector separation (the same color coding for both plots).

distance, and the new contour plot is shown in Fig. 9(c). This plot also features the contour lines of interest (0.9 and 0.95, the latter in white). Intersection of the contour lines with the corresponding distance values on Y-axis not only produces the correct values of $\Delta\lambda$ from X-axis but the outermost values of the wavelengths that were used to compute $\Delta\lambda$ The same prediction can be made from the similar plot obtained from radiance modeling. Presenting a plot for analogous angular predictions is more challenging because it requires combining data from angular, wavelength, and distance domains. The curves like those in Fig. 9(a) and 9(b) can be used alone or in some combination to relate observed changes to distance and generate an empirical curve for distance calibration. For example, Fig. 9(d) demonstrates a constructed ratio of $\Delta\lambda/\Delta\theta$ that clearly shows (distance)$^{-1}$ behavior (note a double-log scale). It is understood that in order to implement distance extraction algorithms, a detailed study of the effect of optical properties of the medium on observed trends via either analytical solution of RTE or Monte-Carlo modeling is required. Nevertheless, we believe that the demonstrated experimental results indicate an interesting possibility of using the shape analysis as a tool for distance extraction.
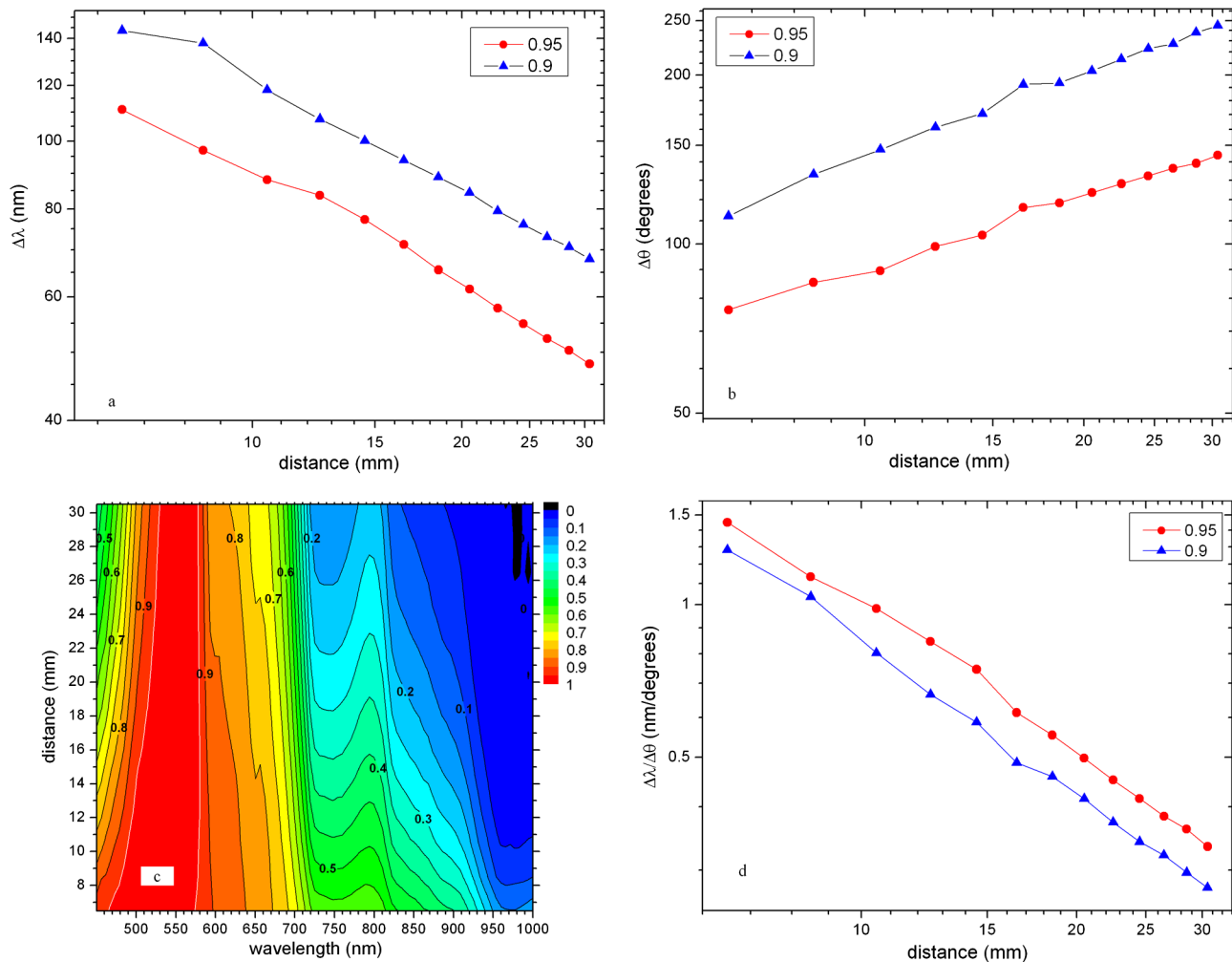
Fig. 9 Distance dependence for the spectral, $\Delta\lambda$ (a) and angular, $\Delta\theta$ (b) ranges produced by contour lines at 0.9 and 0.95 levels of the experimental spectro-angular contour plots. Part (c) shows a spectro-spatial contour plot that correctly predicts $\Delta\lambda$ (contour line for 0.95 level is in white) Part (d) shows a ratio of $\Delta\lambda/\Delta\theta$.

4 Conclusions

We have introduced and analyzed a new spectro-angular form of radiance data that can be used as a platform for developing radiance-based tissue diagnostics and potentially, imaging systems. The approach uncovers details of photon distributions in spectral and angular domains in turbid media and helps to track changes with distance. We demonstrate that spectro-angular mapping has strong foundations in the radiative transfer theory, and all experimental results including complex surface and contour plots agree with radiance modeling using P_∞ approximation for the analytical solution of the RTE. While the experimental approach is not bound by any approximations, distance dependent radiance measurements can be treated under diffusion approximation extracting the effective attenuation coefficient for Intralipid-1% based phantoms. The effective attenuation coefficient plays a major role in determining the shape of the optical distribution and the rate of change with distance. Radiance profiles do not preserve a constant spectral shape at various source-detector separations. Spectral variations are consistent with an increased effective optical path of photons and as result, interaction with a greater number of chromophores. It was demonstrated that shape analysis of spectro-angular contour plots has a potential for extracting

source-detector distance information. We believe that our approach provides new insight into the interpretation of measured angular optical data in turbid media and lays down a foundation for application of spectro-angular mapping for tissue diagnostics and potentially, imaging. The most favorable minimally invasive application would be prostate diagnostics via illumination through rectum and detection through urethra. While the focus of this article is on optical distributions in homogenous phantoms, the approach can be extended to detection and characterization of localized inhomogenieties in turbid media, including biological tissues.

References

1. O. Barajas et al., "Monte Carlo modelling of angular radiance in tissue phantoms and human prostate: PDT light dosimetry," *Phys. Med. Biol.* **42**(9), 1675–1687 (1997).
2. D. Dickey et al., "Radiance modelling using the P3 approximation," *Phys. Med. Biol.* **43**(12), 3559–3570 (1998).

3. D. J. Dickey et al., "Light dosimetry using the P3 approximation," *Phys. Med. Biol.* **46**(9), 2359–2370 (2001).
4. L. C. L. Chin, W. M. Whelan, and I. A. Vitkin, "Information content of point radiance measurements in turbid media: implications for interstitial optical property quantification," *Appl. Opt.* **45**(9), 2101–2114 (2006).
5. L. C. L. Chin et al., "Interstitial point radiance spectroscopy of turbid media," *J. Appl. Phys.* **105**(10), 102025 (2009).
6. H. J. van Staveren et al., "Light-scattering in Intralipid-10 in the wavelength range of 400-1100 nm," *Appl. Opt.* **30**(31), 4507–4514 (1991).
7. J. E. Choukeife and J. P. L 'Huillier, "Measurements of scattering effects within tissue-like media at two wavelengths of 632.8 nm and 680 nm," *Lasers Med. Sci.* **14**(4), 286–296 (1999).
8. G. Zaccanti, S. Del Bianco, and F. Martelli, "Measurements of optical properties of high-density media," *Appl. Opt.* **42**(19), 4023–4030 (2003).
9. A. Dimofte, J. C. Finlay, and T. C. Zhu, "A method for determination of the absorption and scattering properties interstitially in turbid media," *Phys. Med. Biol.* **50**(10), 2291–2311 (2005).
10. J. Jankun et al., "Diverse optical characteristic of the prostate and light delivery system: implications for computer modelling of prostatic photodynamic therapy," *BJU Int.* **95**(9), 1237–1244 (2005).
11. T. C. Zhu, J. C. Finlay, and S. M. Hahn, "Determination of the distribution of light, optical properties, drug concentration, and tissue oxygenation in-vivo in human prostate during motexafin lutetium-mediated photodynamic therapy," *J. Photochem. Photobiol., B* **79**(3), 231–241 (2005).
12. A. Johansson et al., "Realtime light dosimetry software tools for interstitial photodynamic therapy of the human prostate," *Med. Phys.* **34**(11), 4309–4321 (2007).
13. F. Martelli and G. Zaccanti, "Calibration of scattering and absorption properties of a liquid diffusive medium at NIR wavelengths. CW method," *Opt. Express* **15**(2), 486–500 (2007).
14. S. R. H. Davidson et al., "Treatment planning and dose analysis for interstitial photodynamic therapy of prostate cancer," *Phys. Med. Biol.* **54**(8), 2293–2313 (2009).
15. K. K. H. Wang and T. C. Zhu, "Reconstruction of in-vivo optical properties for human prostate using interstitial diffuse optical tomography," *Opt. Express* **17**(14), 11665–11672 (2009).
16. K. Ren, "Recent developments in numerical techniques for transport-based medical imaging methods," *Commun. Comput. Phys.* **8**(1), 1–50 (2010).
17. T. Durduran et al., "Diffuse optics for tissue monitoring and tomography," *Rep. Progr. Phys.* **73**(7), 076701 (2010).
18. A. Liemert and A. Kienle, "Analytical Green's function of the radiative transfer radiance for the infinite medium," *Phys. Rev. E* **83**(3), 036605 (2011).
19. S. Grabtchak, T. J. Palmer, and W. M. Whelan, "Spatially-resolved probing of biological phantoms by point-radiance spectroscopy," *Proc. SPIE* **7894**, 78940A (2011).
20. S. Grabtchak, T. J. Palmer, and W. M. Whelan, "Detection of localized inclusions of gold nanoparticles in Intralipid-1% by point-radiance spectroscopy," *J. Biomed. Opt.* **16**(7), 077003 (2011).
21. S. Grabtchak, T. J. Palmer, and W. M. Whelan, "Radiance spectroscopy tool box for characterizing Au nanoparticles in tissue mimicking phantoms as applied to prostate," *J. Cancer Sci. Ther.* **S1** (2011).
22. R. Michels, F. Foschum, and A. Kienle, "Optical properties of fat emulsions," *Opt. Express* **16**(8), 5907–5925 (2008).
23. F. Foschum, M. Jäger, and A. Kienle, "Fully automated spatially resolved reflectance spectrometer for the determination of the absorption and scattering in turbid media," *Rev. Sci. Instrum.* **82**(10), 103104 (2011).
24. G. M. Hale and M. R. Querry, "Optical constants of water in 200-nm to 200-μm wavelength region," *Appl. Opt.* **12**(3), 555–563 (1973).
25. F. Martelli et al., "Accuracy of the diffusion equation to describe photon migration through an infinite medium: numerical and experimental investigation," *Phys. Med. Biol.* **45**(5), 1359–1373 (2000).
26. J. Swartling et al., "System for interstitial photodynamic therapy with online dosimetry: first clinical experiences of prostate cancer," *J. Biomed. Opt.* **15**(5), 058003 (2010).